

# Path-dependency and emergent computing under vectorial driving

C.M. Meulblok,<sup>1,2</sup> A. Singh,<sup>1,2</sup> M. Labousse,<sup>1,2,3</sup> and M. van Hecke<sup>1,2</sup>

<sup>1</sup>*Huygens-Kamerlingh Onnes Lab, Universiteit Leiden,  
P.O. Box 9504, NL-2300 RA Leiden, Netherlands*

<sup>2</sup>*AMOLF, Science Park 104, 1098 XG Amsterdam, Netherlands*

<sup>3</sup>*Gulliver, CNRS, ESPCI Paris, Université PSL, 75005 Paris, France*

(Dated: March 12, 2025)

The sequential response of frustrated materials—ranging from crumpled sheets and amorphous media to metamaterials—reveals their memory effects and emergent computational potential. Despite their spatial extension, most studies rely on a single global stimulus, such as compression, effectively reducing the problem to scalar driving. Here, we introduce vectorial driving by applying multiple spatially localized stimuli to explore path-dependent, sequential responses. We uncover a wealth of phenomena absent in scalar driving, including non-Abelian responses, mixed-mode behavior, and chiral loop transients. We find that such path dependencies arise from elementary motifs linked to fold singularities, which connect triplets of states—ancestor, descendant, and sibling; and develop a general framework using pt-graphs to describe responses under any vectorial driving protocol. Leveraging binarized vectorial driving, we establish a natural connection to computation, showing that a single sample can encode multiple sequential Boolean circuits, which are selectable by driving strength and reprogrammable via additional inputs. Finally, we introduce graph-based motifs to manage the complexity of high-dimensional driving. Our work paves the way for strategies to explore, harness, and understand complex materials and memory, while advancing embodied intelligence and in-materia computing.

## I. INTRODUCTION

A central goal of condensed matter physics is to describe and understand how materials respond to external stimuli. This is particularly challenging for frustrated, multistable materials, such as amorphous solids or crumpled sheets [1–11]. Their state does not only depend on the current driving, but also on the driving history, leading to a wealth of memory effects which classify materials and give insight into their underlying physics [12, 13]. Examples of such memory effects include measuring after how many driving cycles the response becomes periodic [2, 9, 14–22], or whether the material returns to a previous state when the driving returns to an earlier extremum [9, 10, 23–25]. More complex memory effects can be leveraged to realize *in materia* computing, where the materials state represents the outcome of a calculation, and the initial state and driving history its input [22, 24].

So far, studies of memory and computing have focused on driving with a single driving field, such as global compression or shear. For such *scalar*, quasistatic driving of athermal materials, transition graphs are emerging as a powerful tool for characterizing memory effects [9, 14, 15, 23–33]. These represent states as nodes and irreversible transitions under sweeps of the driving parameter  $\varepsilon$  as edges. They encode the response to any sequential driving protocol, thus allowing to precisely characterize memory effects and emergent computational capabilities [24, 27].

However, the spatial extension of complex materials naturally leads to the question of spatially textured driving. For example, one can push a crumpled sheet at various locations in various orders. We refer to this as *vectorial* sequential driving, with each component of  $\vec{\varepsilon}$  corre-

sponding to, e.g., the compression or strain at a given location. For strongly nonlinear responses, associated with complex materials, superposition no longer describes the response. Instead the driving *path* from  $\vec{\varepsilon}_1$  to  $\vec{\varepsilon}_2$  plays a crucial role, leading to sequential responses, memory effects and computational capabilities that have no counterpart in scalar driving. While path-dependencies have been studied extensively for materials that exhibit plasticity [34], here we focus on path-dependencies of multistable, athermal materials that are driven quasistatically, for which we lack a coherent description.

We address the following broad questions: What new phenomena, memory effects and computational capabilities can be accessed with vectorial driving? How can path-dependent sequential responses be described? How can the descriptions for scalar and vectorial driving be connected? How to deal with the complexity associated with high-dimensional driving?

To address these questions, we combine experiments with simulations and theory to probe the path-dependent sequential response of metamaterials based on chains of coupled nonlinear units (Fig. 1a). These chains naturally allow vectorial driving by compressing the individual units. By designing the units as oppositely biased elastic beams, the metamaterial forms a chain of tunable double-well elements with antagonistic nearest neighbor interactions which captures generic features of the path-dependent response of complex materials.

We start by investigating a short chain comprising two coupled units (Sec. II). By comparing the evolution of a given initial state under different driving paths with the same initial and final driving, we uncover two hallmarks of path-dependency: a *non-Abelian* response, where the final state depends the path, and a *mixed-mode*

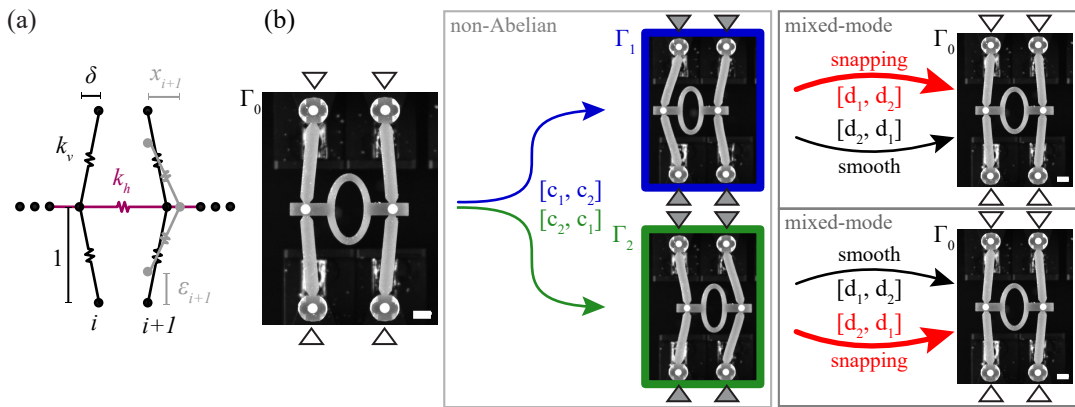


FIG. 1. Geometry and phenomenology. (a) Metamaterial consisting of a staggered chain of  $n$  left-right symmetry broken units (here  $i$  and  $i + 1$ ). Each unit consists of two nearly vertical elastic elements (spring constant  $k_v$ ), and neighboring units are coupled with elastic elements (spring constant  $k_h$ ). The material is driven by a vectorial strain  $\vec{\varepsilon}$ , consisting of vertical strains  $\varepsilon_i$  applied independently by compressing each unit. We non-dimensionalize lengths by the distance between the endpoints of each unit at rest,  $2\ell_0 = 2$ , and specify the configuration by the (non-dimensional) horizontal displacements  $\vec{x} = (x_1, x_2, \dots)$ . The essential design parameters are the dimensionless symmetry breaking  $\delta = x_i(\varepsilon_i = 0)$  and spring ratio  $k := k_h/k_v$ . (b) Left: top view of the experimental sample A in its rest configuration  $\Gamma_0$  ( $n = 2$ ,  $k \approx 0.09$  and  $\delta \approx 0.08$ , scalebar: 5 mm; see Appendix A for details). The central ellipse materializes a soft horizontal spring, and the top and bottom of the vertical beams connect to the strain apparatus, where white and gray triangles indicate relaxed and compressed boundaries. Middle and Right: illustration of two hallmarks of path dependency, under sequential compression respectively decompression of the first and second unit ( $c_1, c_2$  resp.  $d_1, d_2$ ). Middle: a non-Abelian response where the final configuration  $\Gamma_1$  obtained by compression path  $[c_1, c_2]$  (green) differs from configuration  $\Gamma_2$  obtained by compression path  $[c_2, c_1]$  (blue). Right: Mixed mode response where the response is smooth (black) or non-smooth (red) depending on the sequence of the decompression path.

responses, where the nature of the evolution - reversible, continuous or irreversible, discontinuous - depends on the path. We show that fold singularities govern path dependency, and that paths crossing them link three states - ancestor, descendant, and sibling - leading to ADS-triplets that form the elementary unit of path-dependency.

Based on these triplets, we present a general framework which allows to encode the sequential response to *any* vectorial driving protocol (Sec. III). This framework uses strain maps to label the location of fold singularities in driving space, and path-transition graph (pt-graphs) which extend the notion of t-graphs developed for scalar driving. We show that while pt-graphs under scalar driving can be mapped to t-graphs, pt-graphs for higher dimensional driving have qualitatively distinct features.

To enable the experimental characterization of path dependencies under high-dimensional driving (i.e., many inputs), we introduce binarized on/off driving protocols. These protocols focus on paths connecting strains  $\vec{\varepsilon} := \varepsilon^M \vec{b}$ , where  $\varepsilon^M$  is the overall strain and  $\vec{b}$  is a binary vector (Sec. IV). The response can then be captured by ‘b-graphs’ that are simpler than the pt-graphs, and facilitate a natural link between to sequential computing with Boolean circuits. Strikingly, we show that a single sample embeds multiple circuits which can be selected by the strain scale  $\varepsilon^M$ .

We then analyze larger samples and determine the b-graphs as a function of the driving scale  $\varepsilon^M$  for a four-unit chain (Sec. V). To analyze the ensuing complex response, we develop the notion of motifs, that are ‘low dimensional

building blocks’ of the b-graph. Edge motifs consider driving paths restricted to one-dimensional subspaces of  $\vec{\varepsilon}$ , and we show that these are composed of elementary ADS-motifs. Loop motifs, linked to loop-like paths in two-dimensional subspaces, are highly diverse—our four-unit example shows 13 distinct types. They capture a broad range of path dependencies, including the elementary mixed-mode and non-Abelian responses.

We analyze the loop motifs to uncover emergent memory effects and computational capabilities of our samples (Sec. VI). We introduce chiral loop transients where the transient time - i.e. the number of driving loops before the response becomes periodic - depends on the orientation of the loop. This exemplifies the notion of memory effects that have no counterpart for scaling driving. Finally, by splitting the binarized driving at the four inputs of our sample in two for computation, and two for ‘programming’, we show that a single sample can be reprogrammed to mimic a variety of sequential Boolean circuits - on top of the variety that is accessible by varying the magnitude of these drivings.

Together, our findings uncover the elementary motifs that underlie path-dependent behavior in multi-stable systems. While we focus on mechanics, our approach can be applied to any multi-stable system under athermal and quasi-static driving. Vectorial driving thus opens new avenues to characterize frustrated systems, to observe new classes of multi-dimensional responses and memories, and to develop strategies for powerful *in-materia* computing.

## II. SYSTEM AND PHENOMENOLOGY

We introduce chain-like multistable metamaterials that readily enable compression at multiple locations, along with a corresponding minimal spring model (Sec. II A). We investigate a short chain and compare the response to pairs of strain paths that have the same initial and final strains (Sec. II B). We identify two archetypical scenarios for the path-dependent response under vectorial sequential driving: First, a *non-Abelian* response, where the final configuration depends on the strain path (Sec. II B 1); second, a *mixed-mode* response, where the response is either smooth or non-smooth, depending on the strain path (Sec. II B 2). Both can be understood to arrive from a fold bifurcation, which links three configurations that we term ancestor, descendant and sibling (Sec. II B 3).

### A. Metamaterial, Strain Protocols and Model

*Design.*— We aim to realize a metamaterial that naturally allows compression at multiple locations, is scalable, can be multistable, and features path dependent responses. To meet these requirements, we investigate a chain-like geometry of  $n$  units that each have a strongly nonlinear response and can become bistable. We design such a geometry based on a spring chain, consisting of  $n$  vertical units that each contain two equal springs meeting in a central node that acts as a hinge. Neighboring units are coupled by a horizontal spring between these nodes. The horizontal positions of the ends of the units are fixed such that in their relaxed state, the units are not perfectly vertical but alternately kink left and right (Fig. 1a). This configuration ensures a deterministic response when the ends of the units are compressed vertically. Moreover, if one unit is compressed sufficiently to flip the orientation of the kink of its neighbor, we anticipate that first compressing unit  $i$  and then  $i + 1$  results in a different configuration than first compressing unit  $i + 1$  and then  $i$ : this multistable metamaterials has a path dependent response (Fig. 1b).

*Sample Geometry.*— Experimentally, we realize metamaterials based on this design in flexible silicone rubber using standard 3D printing and molding techniques (see appendix A). Each unit  $i$  consists of two connected, nearly vertical elastic beams of stiffness  $k_v$  which are coupled by horizontal beams of spring constant  $k_h$ ; the ratio  $k := k_h/k_v$  is an important parameter. The beams have tapered connections to minimize torques. As we are interested in the limit where  $k \ll 1$ , we realize the soft horizontal springs using an elliptical annulus (Fig. 1b). The distance between the endpoints of each unit at rest,  $2\ell_0$ , defines the lengthscale  $\ell_0$  that we use to non-dimensionalize all lengths. The units are pre-kinked over a (non-dimensional) distance  $\delta$ , such that their rest positions (defined as the horizontal deviation from the units midpoint) are  $x_i = (-1)^{i+1}\delta$  (this requires the

beams rest length to be  $1 + \delta^2/2$ ). We focus here on geometries with  $\delta \approx 0.08$  and  $k \approx 0.09$ , and create samples with  $n = 2$  and  $n = 4$  units (see appendix A).

*Strain protocols.*— We use a custom-made device to control the spatially localized compressive strains  $\varepsilon_i$  with accuracy  $\sim 10^{-3}$  by symmetrically shortening the end-to-end distances  $2\ell = 2\ell_0(1 - \varepsilon_i)$  such that all nodes remain horizontally aligned. We use quasi-static driving (strain rate is  $5 \cdot 10^{-4} \text{ s}^{-1}$ ) and track the real-space configuration of the structure given by  $\vec{x} = (x_1, x_2, \dots)$  using a CCD camera, resulting in an accuracy in  $x_i$  of 0.002 (see appendix A). Together, our set-up allows for automated driving protocols and precise measurements of the configurational response.

We consider strain paths  $P$  that quasistatically ramp the input strains  $\vec{\varepsilon} = (\varepsilon_1, \varepsilon_2, \dots)$  between sequences of specific points in strain-space. While we also consider general driving protocols, we often employ 'binary' paths that consists of sequences of elementary compressions  $c_i$  (increase of  $\varepsilon_i$  from a minimum value  $\varepsilon_i^m$  to a maximum value  $\varepsilon_i^M$ ) and decompressions  $d_i$  (decrease of  $\varepsilon_i$  from  $\varepsilon_i^M$  to  $\varepsilon_i^m$ ) while the other strains are kept fixed. In many cases we take  $\varepsilon_i^m = 0$  and  $\varepsilon_i^M = \varepsilon^M$ , so that  $\varepsilon^M$  sets an overall strain scale. Finally, we denote sequences of compression and decompression steps using square brackets, e.g.,  $[c_1, c_2, d_1, d_2]$  represents a loop-like compression path (read from left to right).

*Minimal Model.*— In addition to the experiments, we numerically explore a spring model. We model each beam as a linear spring with freely rotating hinges, use equidistance vertical compression points, and break the left-right symmetry by taking horizontal springs with alternating rest length  $1 + (-1)^i 2\delta$  (Fig. 1a). Expanding the elastic energy to the lowest order in  $x_i$  yields:

$$E = \sum_{i=1}^n \left( \frac{x_i^2}{2} - \gamma_i \right)^2 + \sum_{i=1}^{n-1} \frac{k}{2} (x_i - x_{i+1} - (-1)^i 2\delta)^2, \quad (1)$$

where  $\gamma_i := \varepsilon_i + \delta^2/2 - \varepsilon_i^2/2 \approx \varepsilon_i + \delta^2/2$ . The first term describes the tuneable quartic potential of each unit, and the second term describes the interactions and lifts the units degeneracy to make the response deterministic. In the limit of small  $\delta$ , one can rescale the parameters to eliminate  $\delta$ , leaving the effective interaction strength  $k$  as the main system-dependent parameter (see Appendix B).

### B. Path dependency

Here we explore path dependency for a two-unit sample (A), and demonstrate two paradigmatic forms of path-dependency which have no counterpart under scalar driving: a non-Abelian response and a mixed-mode response.

### 1. Non-Abelian Response

We consider a pair of sequential driving paths  $P_1 : [c_1, c_2]$  and  $P_2 : [c_2, c_1]$ , with  $\varepsilon_i^m = 0$  and  $\varepsilon_i^M = \varepsilon^M = 0.03$ . The sample is initially relaxed ( $\vec{\varepsilon} = 0$ ) in the unique rest configuration  $\Gamma_0$ , such that the driving paths  $P_1$  and  $P_2$  produce smooth deformations until the final configurations  $\Gamma_1 = P_1(\Gamma_0)$  and  $\Gamma_2 = P_2(\Gamma_0)$  are reached. We compare the final configurations  $\Gamma_1$  and  $\Gamma_2$  and find  $\Gamma_1 \neq \Gamma_2$ , demonstrating path dependence (Fig. 1b). Since  $\Gamma_1$  and  $\Gamma_2$  experience the same strain  $\vec{\varepsilon} = (\varepsilon^M, \varepsilon^M)$ , this non-Abelian response necessitates bistability. Similar non-Abelian behaviors have recently been observed in various other strongly nonlinear, multi-stable metamaterials under sequential compression [35–37].

In our system, which was designed with such behavior in mind, this non-Abelian response is observed for a large range of strains (see Sec. IV). This behavior can intuitively be understood from the left ( $x_i < 0$ ) or right ( $x_i > 0$ ) leaning orientations of the units. Consider the evolution of the real-space configuration  $\{x_i\}$  during  $P_1$  (Fig. 1b; see Movie S1). In the first stage ( $c_1$ ), unit 1 compresses leftward, pulling unit 2 to lean left as well. Further compression of unit 2 in stage two ( $c_2$ ) pushes both units left, making the resulting configuration  $\Gamma_1$  left-leaning. By contrast, in  $P_2$ , compression of unit 2 shifts unit 1 rightward, yielding a right-leaning  $\Gamma_2$  (Fig. 1b). We note, however, that such orientation changes are not required to observe a non-Abelian response: intermediate values of  $\varepsilon^M \approx 0.011$  lead to a more subtle non-Abelian regime without changes in the units orientations (Appendix C).

### 2. Mixed-mode response

Next, we follow the configurations during the decompression paths  $P_3 : [d_1, d_2]$  and  $P_4 : [d_2, d_1]$ . Starting from either of the configurations in the bistable regime at  $\vec{\varepsilon} = (\varepsilon^M, \varepsilon^M)$ , both paths  $P_3$  and  $P_4$  lead to the same configuration, i.e.,  $P_3(\Gamma_1) = P_4(\Gamma_1) = \Gamma_0$  and  $P_3(\Gamma_2) = P_4(\Gamma_2) = \Gamma_0$ . However, whereas  $P_4(\Gamma_1)$  leads to a smooth deformation,  $P_3(\Gamma_1)$  features a non-smooth, irreversible transition — and similarly for  $P_3(\Gamma_2)$  and  $P_4(\Gamma_2)$  (Fig. 1b; see Movie S2)<sup>1</sup>. This mixed-mode response represents a different type of path-dependency than the non-Abelian response.

### 3. Fold bifurcation

To understand the root cause of the non-Abelian and mixed mode response, we follow the evolution of the configurations  $\Gamma_1$  and  $\Gamma_2$  between strains starting from  $(\varepsilon^M, \varepsilon^M)$  to  $(0, \varepsilon^M)$  (Fig. 2a). Our data shows that the irreversible transition is associated with a fold bifurcation, and this is confirmed in our numerical model where we can follow both stable and unstable configurations (Fig. 2b). As we argue below, this situation exemplifies the central motif that causes path dependencies in multi-stable materials: On one side of the fold curve, there are two types of configurations (ancestor and sibling). Moving across the fold curve, the ancestor vanishes, and the system then jumps to another configuration that we call the descendant. Note that while descendant and sibling are smoothly connected, they can be distinguished by the presence of the ancestor, or equivalently, their strain in comparison to the fold transition. Hence, three configurations - that we refer to as ancestor, descendant and sibling - are connected by an irreversible (fold) transition from the ancestor to the descendant and a reversible transition between the descendant and sibling (Fig. 2c-d).

## III. GENERAL APPROACH FOR SEQUENTIAL VECTORIAL DRIVING

We present a general framework to describe the response for arbitrary driving paths, based on the central role that fold singularities and ADS triplets play, and illustrate our approach using sample A (Sec. III A). We then discuss the relations and differences between the pt-graph framework for vectorial driving and the t-graph description for scalar driving (Sec. III B). We show that the scalar description is a special case of the general vectorial description, and that for higher dimensional driving pt-graphs have unique features not present for scalar driving.

### A. Strain Maps and PT-Graphs

To describe the response to *any* generic driving path, we introduce strain maps and path-transition graphs (pt-graphs). Strain maps encode the location of the fold singularities in driving space, and pt-graphs describe transitions between states that occur when the driving path crosses one of these fold singularities. Hence, nodes and edges of the pt-graph describe states and their transition, and the edges are labeled by their respective fold singularity. The edges either are directed, corresponding to irreversible transitions (such as the path from ancestor to descendant) or undirected, corresponding to reversible, smooth transitions (such as path between descendant and sibling). Constructing this description requires three steps: first identify the strain map; second, use it

<sup>1</sup> While here the discontinuous transition is associated with decreasing strain, we will later also encounter discontinuous transitions under increasing strain.

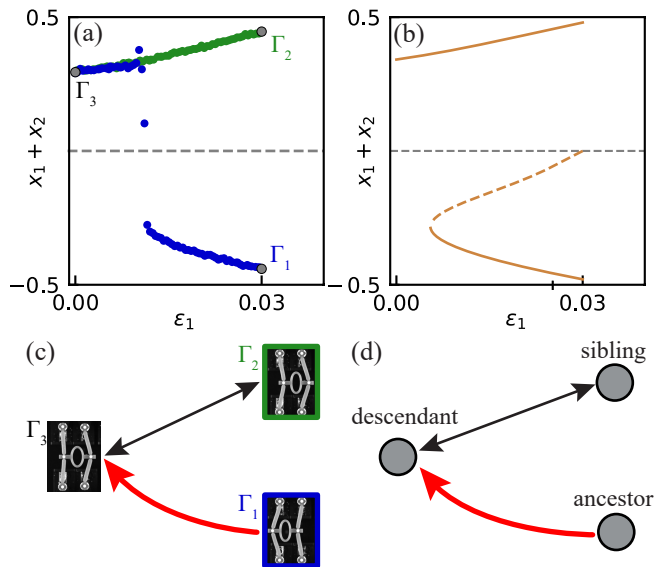


FIG. 2. Fold bifurcation and ADS-triplet (a-b) Evolution of the configuration  $\vec{x}$  of sample A as a function of strain  $\varepsilon_1$  which is lowered from 0.03 to 0, projected on the collective coordinate  $x_1 + x_2$ ; here we fix  $\varepsilon_2 = \varepsilon^M = 0.03$ . (a) Experimental data for sample A; we initialize the sample in configurations  $\Gamma_1$  and  $\Gamma_2$  using the strain paths shown in Fig. 1b. (b) Simulations of the corresponding spring model, where  $\varepsilon_1$  is both increased and decreased, showing stable (full) and unstable (dashed) solutions, thus revealing a fold singularity. (c-d) Graph representation of the general structure underlying path dependency: three configurations (ancestor, descendant and sibling) are connected by reversible (black) and irreversible (red) transitions;  $\Gamma_1$  is the ancestor,  $\Gamma_3$  the descendant, and  $\Gamma_2$  the sibling.

to define states; and third determine the pt-graph — for more details, see [38].

We first obtain the strain map for sample A by determining the locus in strain space of the fold singularities that govern the irreversible transitions for  $0 \leq \varepsilon_i \leq 0.04$  (Fig. 3a). To do so, we explore CCW and CW loop-like driving protocols,  $P_5 : [c_1, c_2, d_1, d_2]$  and  $P_6 : [c_2, c_1, d_2, d_1]$ ; in  $P_5$  ( $P_6$ ) we fix  $\varepsilon_1^M = 0.04$  ( $\varepsilon_2^M = 0.04$ ) and sweep  $\varepsilon_2^M$  ( $\varepsilon_1^M$ ). Using  $P_5$ , we obtain the locus of the irreversible transitions ( $f$ ) from ‘left-leaning’ to ‘right-leaning’ configurations;  $P_6$  allows to define the irreversible transitions ( $g$ ) from ‘right-leaning’ to ‘left-leaning’ configurations (Fig. 3a). The curves  $f$  and  $g$  thus specify the location of the fold singularities in strain space. For this specific example,  $f$  and  $g$  meet in a singular point  $Q$  that corresponds to a cusp singularity, associated with a pitchfork bifurcation from a symmetric configuration where  $x_1 = -x_2$  to a pair of asymmetric configurations (Fig. 3a; Appendix C).

Second, for a given range of strains, the strain map partitions the strain space into domains. We define states as equivalence classes of configurations that are smoothly connected *within each domain*. For this example, the fold curves  $f$  and  $g$  partition the strain space into a monos-

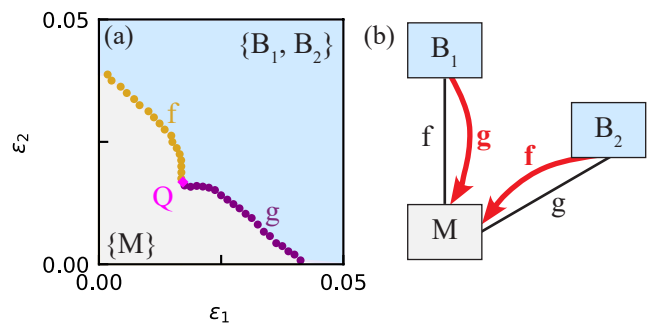


FIG. 3. The path dependent response described by a strain map (a) and pt-graph (b), here for sample A ( $n = 2, k \approx 0.09$ ). (a) The locations of the fold transitions  $f$  and  $g$  form curves of codimension one that separate the strain space into a monostable domain with state  $M$  (gray) and a bistable domain with states  $B_1$  and  $B_2$  (blue). The curves  $f$  and  $g$  meet in point  $Q$  which corresponds to a codimension-two cusp singularity, or pitchfork bifurcation (Appendix C). (b) The pt-graph describes the smooth reversible connections (undirected black edges) and discontinuous irreversible transitions (directed red edges) for strain paths that cross the respective fold singularities of the strain map.

table domain and a bistable domain, leading to three states (Fig. 3a). The evolution of the configuration in the monostable domain is smooth and reversible, and we thus associate all these configurations with a state  $M$ . In the bistable domain, we find two stable configurations for any value of the strain. These two configurations smoothly deform along strain paths within the bistable domain, defining two states  $B_1$  and  $B_2$  - note that configurations associated with states  $B_1$  and  $B_2$  cannot smoothly deform into each other for strain paths within the bistable domain. In passing, we note that our definition of states as configurations smoothly connected within domains explains why we distinguish between the descendant and sibling: these two states correspond to smoothly connected configurations but in two different domains. Hence, the locus of the fold bifurcations determines a strain map and defines the states; for the example, the strain map has two fold curves (Fig. 3) and three states ( $M, B_1$  and  $B_2$ ).

Third, to specify the full path dependent response, we construct a pt-graph. The nodes of this mixed graph correspond to the states  $M, B_1$  and  $B_2$ , and its edges correspond to paths that cross one of the fold singularity curves, and are labeled accordingly. The pt-graph combines directed and undirected edges. The undirected edges correspond to smooth, reversible paths between descendant and sibling states that, while smoothly connected, occur in different domains in strain space; the directed edges correspond to non-smooth, irreversible paths from an ancestor state to a descendant state. Hence, to construct the pt-graph we determine how states are connected when *crossing* the fold curves (in this paper we ignore singular paths, such as paths crossing through  $Q$ ). For our specific example, the situation is simple.

State  $M$  smoothly transforms into state  $B_1$  when we cross from the monostable to the bistable domain across  $f$ , and smoothly transforms into state  $B_2$  across  $g$ ; these smooth paths are reversible, so that  $B_1$  and  $B_2$  smoothly connect to  $M$  across  $f$  and  $g$ , respectively. The irreversible transitions occur when starting in the bistable domain. For instance, beginning in state  $B_1$ , crossing boundary  $g$  leads to an irreversible transition to  $M$  ( $B_1 \rightarrow M$ ). Similarly, crossing boundary  $f$  results in the irreversible transition  $B_2 \rightarrow M$  (Fig. 3).

The combination of the strain map and the pt-graph together captures the general features of the path dependent response in multistable systems for *any* generic strain path (i.e., not crossing singular points such as  $Q$ ). This provides a unified framework to describe non-Abelian and mixed-mode responses, as well as transient and complex memory effects under vectorial sequential driving. In particular, they allow to determine precisely when certain types of responses occur: starting from any configuration associated with state  $M$ , a non-Abelian response occurs for two paths that either cross  $f$  or  $g$  and meet in the bistable domain. Similarly, starting from any configuration associated with  $B_1$  or  $B_2$ , a mixed-mode response occurs for pairs of strain paths that cross  $f$  or  $g$  and meet in the monostable domain.

## B. PT-Graphs: General Features

The example above illustrates general features of pt-graphs. First, each fold curve is associated with an ancestor, descendant, sibling (ADS) triplet. In particular,  $(B_2, M, B_1)$  are the ancestor, descendant and sibling associated with curve  $f$ , which we denote as  $ADS_f = (B_2, M, B_1)$ ; similarly,  $ADS_g = (B_1, M, B_2)$ . Second, the topology of the strain map constrains the number of edges in the pt-graph as each state and each adjacent fold-boundary correspond to an outgoing edge in the pt-graph. Hence, the number of outgoing edges is  $\Sigma_{\text{domain}} n_s n_f$ , where  $n_s$  and  $n_f$  are the number of states and adjacent fold curves per domain, respectively; here  $\Sigma_{\text{domain}} n_s n_f = 6$ . As reversible edges in the pt-graph correspond to a pair of incoming and outgoing edges, this implies that  $\Sigma_{\text{domain}} n_s n_f = 2n_r + n_i$ , where  $n_r$  and  $n_i$  are the numbers of reversible and irreversible edges of the pt-graph, respectively. We will discuss pt-graphs for more complex singularities elsewhere [38, 49, 50].

### 1. PT-Graphs vs T-Graphs

Scalar driving is a special case of vectorial driving. Here, we discuss the relation between our pt-graph framework and the t-graphs developed to describe the sequential response under scalar driving [5, 14, 23, 24, 26, 27, 30–32, 39].

The nodes in a t-graph represent states which are equivalence classes of configurations: two configurations

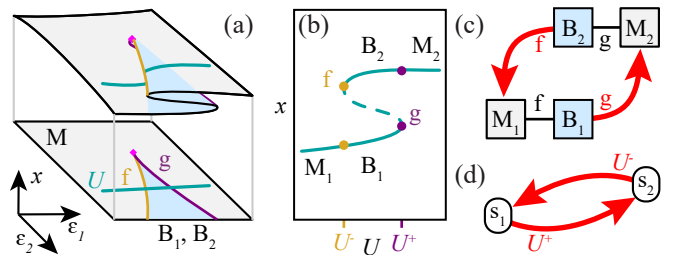


FIG. 4. The relation between pt-graphs and t-graphs. (a) The configuration space near the cusp singularity of sample A, with a one-dimensional path parametrized by  $U$  (green). (b) The collective coordinate  $x$  as a function of the scalar driving  $U$ . (c) Along the one-dimensional path, we can construct a pt-graph. (d) By identifying uniquely, smoothly connected states, we obtain a standard t-graph, with two states and edges labeled by the up- and down-switching thresholds  $U^\pm$ .

correspond to the same state if they smoothly deform into each other under slow increase or decrease of the driving strain  $U$ . The nodes are connected by directed edges that represent irreversible transitions. Each transition is characterized by, first, whether it is an up or down transition, i.e. triggered by increasing or decreasing  $U$ , and second, the switching thresholds  $U^\pm(S)$  [9, 23, 24, 27, 29, 39]. The t-graph with labeled edges specifies the response under any (generic) quasistatic driving protocol.

There are striking similarities between pt-graphs and t-graphs. Both combine a graph and a strain map - for t-graphs the strain map is simply the collection of switching thresholds [24, 39]. Their nodes represent states, and their edges correspond to transitions that occur at a codimension-one subspace of the driving-space: points given by switching thresholds in the case of scalar driving, and fold manifolds for vectorial driving.

However, there are also striking differences. Most importantly is the subtle difference in the definition of what constitutes a state. For vectorial driving, two states can be connected by both a reversible and irreversible transition, associated with two different fold singularities; for scalar driving, this never occurs. Hence, while for scalar driving the group of configurations connected by a smooth deformation form one state, for vectorial driving we define states as groups of configurations that smoothly deform into each other for deformation paths that do not cross any fold transition (see Sec. III A). As a consequence, t-graphs only contain irreversible transitions, whereas pt-graphs contain both reversible and irreversible transitions (Fig. 3).

We now show that t-graphs are a special case of pt-graphs. We illustrate the mapping from a pt-graph with one-dimensional driving to a t-graph by using the example of a cusp singularity as displayed by sample A. Consider the pt-graph along a one-dimensional curve, so that  $\vec{\epsilon}$  is a function of the scalar driving  $U$  (Fig. 4a). As a function of  $U$ , the collective coordinate  $x := x_1 + x_2$  forms an elementary hysteresis loop, constructed by appropriately connecting two fold bifurcations (Fig. 4b).

The fold bifurcations  $f$  and  $g$  occur at switching thresholds  $U^-$  and  $U^+$  and are associated with ADS-triplets:  $ADS_f = (B_2, M_1, B_1)$  and  $ADF_g = (B_1, M_2, B_2)$ . Note that while  $M_1$  and  $M_2$  are the same state in the pt-graph for two dimensional driving (Fig. 3), as there is a smooth path that connects them that does not cross  $f$  or  $g$ , in the pt-graph for one dimensional driving,  $M_1$  and  $M_2$  are not smoothly connected along  $\bar{\varepsilon}(U)$  and form distinct states. Hence, restricted to the one-dimensional path, we obtain a pt-graph with four states, two irreversible edges and two reversible edges (Fig. 4c).

The pt-graph for one dimensional driving can be simplified further by clustering smoothly connected pairs of states in one-dimensional pt-graphs – here  $(M_1, B_1)$  and  $(M_2, B_2)$  — as states  $S_1$  and  $S_2$  (Fig. 4c-d). This procedure is well-defined since the location of the fold singularities form points on a line and are well-ordered; hence states that are connected smoothly cannot be connected irreversibly through a different path. In our example, this clustering results in a t-graph with two states and only irreversible transitions (Fig. 4d). For this example, the t-graph represents a single elementary hysteresis loop. More generally, for any pt-graph that is restricted to a one-dimensional driving subspace, a similar mapping to t-graphs can be constructed: t-graphs are thus special cases of pt-graphs - and pt-graphs generally encode a large number of t-graphs.

We close this section by noting that memory effects under scalar driving can often be understood by considering two-level subsystems, such as bistable springs, and abstracted models of these called hysterons [5, 9, 10, 14, 23–26, 28–32]. A promising avenue for exploration is thus to determine which physical building blocks produce ADS triplets, and how these can be used these to design (meta)materials with targeted sequential responses under vectorial driving.

#### IV. PATH DEPENDENCY AND *IN MATERIA* COMPUTING

The sequential response of multistable systems can be considered as a form of *in materia* computing [24]. The near-binary (left/right) configurations of our beams, suggest to investigate the link between path dependency and sequential Boolean logic. To do so, we project the real-space configuration  $\vec{x}$  onto a binary output variable  $\vec{Q} = (q_1, \dots)$ , where  $q_i = 0$  (1) when  $x_i < 0$  ( $x_i > 0$ ). We introduce a binary input variable  $\vec{b} = (b_1, b_2, \dots)$  with  $b_i = 0, 1$ , defining the strain as  $\varepsilon_i = \varepsilon_i^M b_i$ , and vary  $\varepsilon_i^M$ . We then study how the binary output  $\vec{Q}(\vec{b})$  responds to binary strain paths composed of compression steps ( $c_i$ ) and decompression steps ( $d_i$ ), starting from the neutral configuration  $\vec{Q} = (01)$  at  $\vec{b} = (00)$ <sup>2</sup>. We represent the

path-dependent response  $\vec{Q}(\vec{b})$  using equivalent Boolean circuits (details in Appendix D).

Different responses are found depending on the values of  $\varepsilon_i^M$ . In sample A, there are three relevant strain scales: at  $\varepsilon_1 = \varepsilon_2 = \varepsilon_c \approx 0.017$  there is the cusp singularity; for  $\varepsilon_i^M > \varepsilon_g \approx 0.018$ , compressing a single beam changes the sign of  $x_i$  of the other; and the fold curves terminate at the axes for  $\varepsilon = \varepsilon_{f,i} \approx 0.04$ . In the narrow interval  $\varepsilon_c < \varepsilon_i < \varepsilon_g$ , the binary projection is not suitable (see appendix. C), and we focus on the pathways for  $\varepsilon_i$  outside this interval.

Strikingly, we find five different sequential responses, depending on the strain scales  $\varepsilon_i^M$  (Fig. 5). First, for small  $\varepsilon_i^M < \varepsilon_c$ , the strains are too small to reach the bistable domain and the response is smooth and path independent, yielding a trivial circuit (Fig. 5a). For intermediate strains ( $\varepsilon_g < \varepsilon_i^M < \varepsilon_{f,i}$ ), two stable configurations are reached for  $\vec{b} = (11)$ , resulting in non-Abelian pathways and irreversible transitions (Fig. 5b). This path dependent response is captured by an set-reset-latch (sr-latch), a simple circuit that can store one bit of information [40] (Fig. 5b; for details, see appendix D). For larger strains ( $\varepsilon_i^M > \varepsilon_f$ ), every  $\vec{b} \neq (00)$  produces two stable configurations, which can be represented by a logic circuit preceding the same one-bit memory element (Fig. 5c). Finally, asymmetric protocols where one of  $\varepsilon_1^M$  and  $\varepsilon_2^M$  is in between  $\varepsilon_g$  and  $\varepsilon_f$ , and the other is above  $\varepsilon_f$  can be represented variations of such circuits (Fig. 5d-e). Thus, by selecting the magnitude of the binary strains at either ‘input’, sample A can mimic four related yet distinct non-trivial Boolean circuits.

While this mapping from path dependency to Boolean logic circuits highlights the potential for *in materia* computing with multiple inputs, Boolean circuits are hard to interpret, in particular for larger systems. Moreover, technical issues arise to the frequent occurrence of race-conditions in such circuits – During race conditions, the logic state flips at multiple locations in the circuit simultaneously, leading to sensitivities to tiny differences in their timing. These race conditions are a major reason for the widespread use of clocked, synchronous circuits in digital technology, rather than more frugal, faster and energy efficient asynchronous circuits. Finally, not all physical systems allow natural binarization of their configurations.

We therefore introduce a graph representation of path dependencies to binary inputs (Fig. 5a3-e3). These binary graphs (b-graphs) contain the evolution of the configuration during each possible (de)compression, for a specific fixed set of strain scales  $\varepsilon_i^M$ . Each unique configuration corresponds to a node, and all nodes are grouped according to their respective binary strain  $b_i$ . The smooth or non-smooth evolution during each (de)compression step is represented by undirected and directed edges respectively. A b-graph is thus a mixed graph where each node has  $n$  outgoing edges corresponding to the  $n$  possible binary (de)compression steps, as we show for sample A (Fig. 5a3-e3).

<sup>2</sup> For brevity of notation, we drop commas and write these binary quantities as (00) instead of (0, 0)

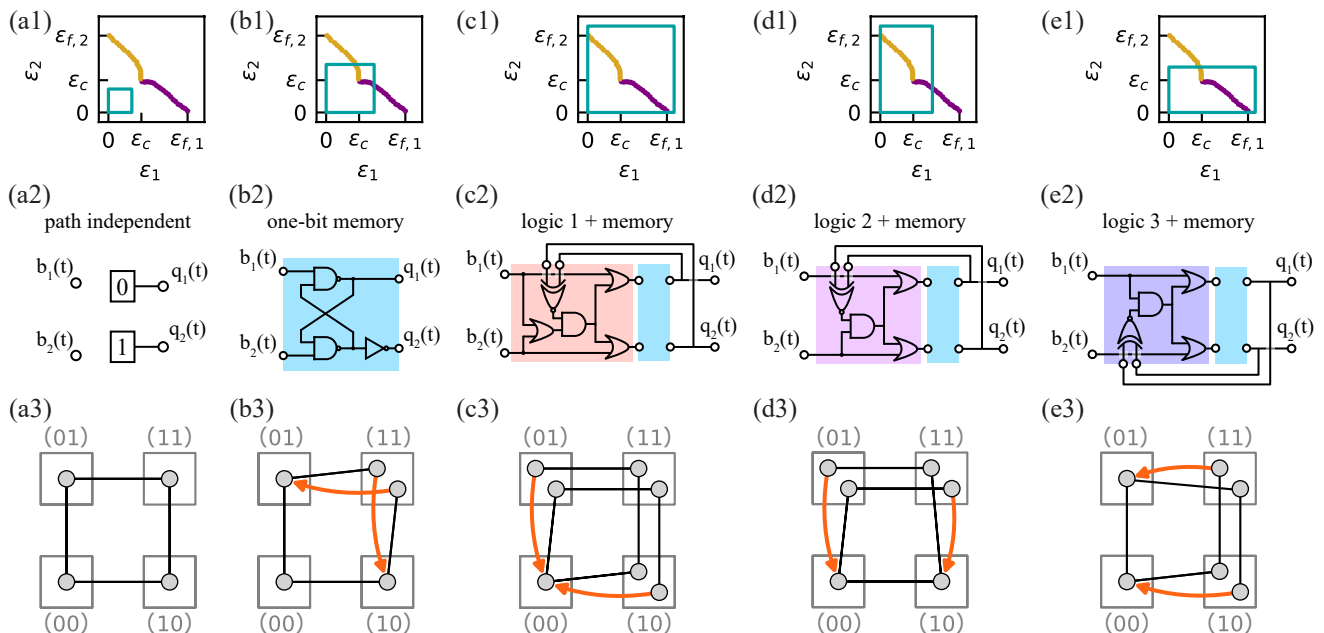


FIG. 5. Sequential response of sample A to binary strain protocols. Top row: fold curves (yellow, purple) and binary strain protocols (green). For sample A,  $\varepsilon_c \approx 0.017$ ,  $\varepsilon_g \approx 0.018$ ,  $\varepsilon_{f,1} \approx 0.039$  and  $\varepsilon_{f,2} \approx 0.041$ . In (a-c), we use symmetric strain scales  $\varepsilon^M = 0.01, 0.025$ , and  $0.045$ , respectively. In (d-e), the binary strain protocols are asymmetric with  $(\varepsilon_1^M, \varepsilon_2^M) = (0.025, 0.045)$  and  $(0.045, 0.025)$ , respectively. Mid row: Corresponding Boolean circuits, where the blue blocks represent rs latches as in b2 (see appendix D for details). Bottom row: Corresponding b-graphs. Here, each node represents a configuration grouped (in squares) by the binary strain  $b_i$  (labeled above or below the squares), and each edge represent a smooth (undirected and black) or irreversible (directed and orange) transition between two configurations.

B-graphs contain a subset of the information in p-graphs. The restriction to binary compression, however, circumvents the challenges associated with obtaining complex strain maps, in particular for higher dimensional strains, and provides a practical, scalable and often natural strategy to explore the saillant features of the path dependent response. In particular, we note that the non-Abelian and mixed-mode response, as well as the ADS motifs, can be represented in b-graphs.

## V. HIGH DIMENSIONAL STRAIN SPACE

For increasing number of units and inputs, the strain space becomes high dimensional and keeping track of all domains and singularity boundaries becomes challenging. In such cases the b-graphs provide a simple alternative to explore path-dependencies.

To illustrate this, we determine the b-graph for a four-unit ( $n = 4$ ) sample B with the same geometrical parameters as sample A ( $k = 0.09$ ,  $\delta = 0.08$ ) at fixed  $\varepsilon_i^M = \varepsilon^M = 0.035$  (Fig. 6a-b). Starting from the initial monostable configuration at  $\vec{b} = (0000)$ , we obtain all reachable configurations by a recursive strategy: First, we apply all  $4!$  compression sequences that reach  $\vec{b} = (1111)$ , yielding 21 distinct configurations. Next, for each of these, we apply any possible single-step decompression, which yields one additional configuration.

We repeat this procedure until no new configurations are discovered, and keep track of the smooth or non-smooth nature of all transitions (see appendix E). This yields a b-graph consisting of  $n_c = 22$  configurations,  $n_s = 35$  smooth transitions, and  $n_i = 18$  irreversible transitions; note that in general,  $2 \cdot n_s + n_r = n \cdot n_c$  (Fig. 6b). We have determined the b-graphs for sample B for some other values of  $\varepsilon^M$  experimentally (appendix E), and will discuss the full diversity of b-graphs observed numerically elsewhere [41]. The crucial point is that a single sample can encompass a myriad of b-graphs.

### A. Motifs

To analyze the b-graphs, we introduce the notion of *motifs*, which can be seen as its 'low dimensional building blocks' (Fig. 6c). Geometrically, binary strains can be represented as vertices of a  $n$ -dimensional hypercube, where the  $2^n$  (here: 16) vertices correspond to  $\vec{b}$ , the  $n \cdot 2^{n-1}$  (here: 32) edges represent the paths between adjacent strains, and the  $n(n-1) \cdot 2^{n-3}$  (here: 24) faces correspond to loops involving (de)compressing two strains. We focus here on *edge motifs*, which capture the qualitative patterns of configurations and transitions between adjacent strains, and *loop motifs*, which describe these patterns associated with the two-dimensional faces (Fig. 6c). We deal with symmetries by considering motifs

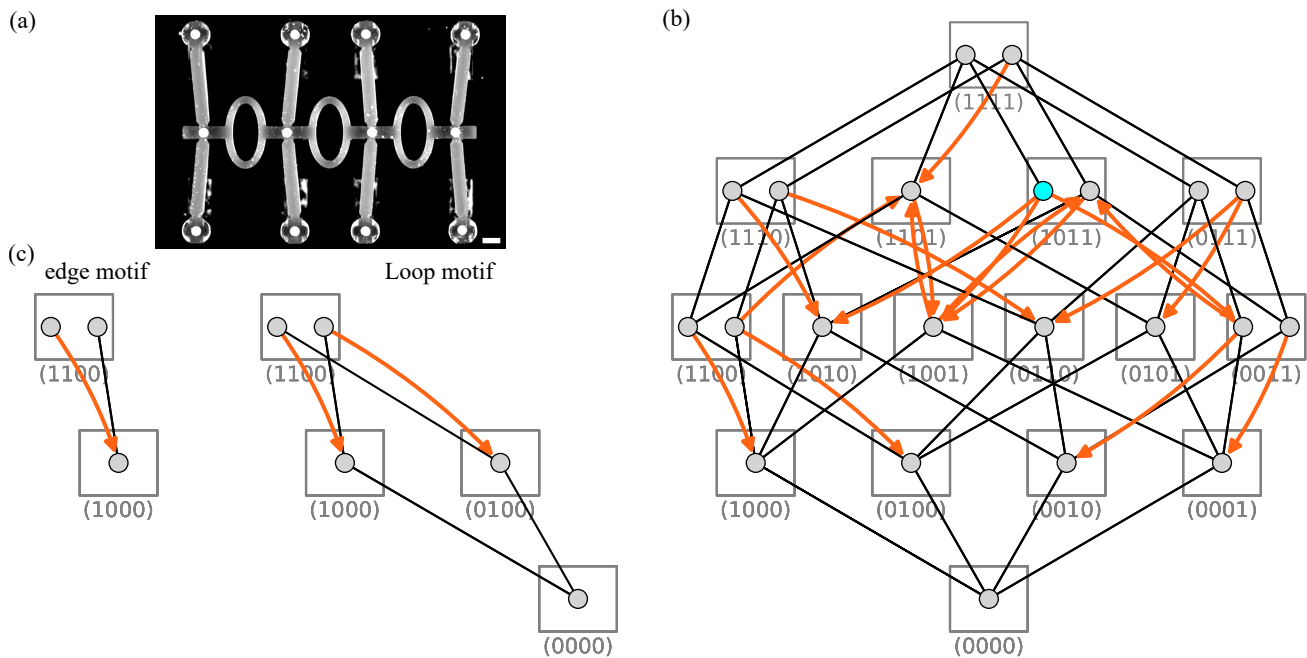


FIG. 6. (a) Four-beam ( $n = 4$ ) sample B (scalebar is 5 mm, see appendix A for details). (b) B-graph for sample B at  $\varepsilon^M = 0.035$ . Each rectangle represents a binary strain  $\vec{b}$  as labeled. We organize all  $2^4$  strain states by  $\sum b_i$  along the vertical axis, and by their lexicographical order along the horizontal axis. The grey configurations are found by sequential compression of the rest-configuration at  $\vec{b} = (0000)$ ; the blue configuration requires one decompression step, e.g.,  $d_2(1111)$ . (c) examples of low-dimensional building blocks (motifs) of the b-graph in (b). left: one-dimensional 'fold' (or 'ADS') edge motif; right: two-dimensional 'non-Abelian' loop motif.

equivalent under flipping of the compression and decompression of each strain, i.e.,  $b_i \leftrightarrow (1 - b_i)$ , and under relabeling of the configurations at a given strain. As we show below, motifs are powerful tools for identifying the main features and distinct path dependencies encoded by the b-graph: for example, sample B exhibits three edge and 10 loop motifs that are absent in the two-beam system, and loop motifs allow to detect the paradigmatic non-Abelian and mixed-mode path dependencies (Fig. 6c).

### 1. Edge motifs

We determined the six edge-motifs of sample B, three of which only occur once (Fig. 7a-f). We refer to the two simplest motifs as the smooth motif and the fold motif (Fig. 7a-b). These motifs are dominant in many b-graphs and, in particular, are the only edge motifs found in the two-beam sample A (Fig. 5). The smooth motif is characterized by a smooth reversible path between two single configurations and arises when there are no fold singularities along the strain path<sup>3</sup> (Fig. 7a). The fold-motif con-

tains a descendant for one strain and an ancestor-sibling pair for the other, and emerges when the path crosses a single fold singularity<sup>4</sup> (Fig. 7b). We note that the descendant can be associated with either the compressed or decompressed strain — compare, e.g., the transitions between  $\vec{e}_b = (1100)$  and  $(1000)$  and between  $\vec{e}_b = (1100)$  and  $(1101)$  (Fig. 6) — and we do not distinguish between these as we consider motifs equivalent under flipping of compression and decompression (Fig. 7b).

The more complex edge-motifs are *reducible* — composed of multiple smooth and fold motifs via juxtaposition and/or concatenation (Fig. 7g-i). The simplest example of a reducible motif is a juxtaposition of motifs, such as the double smooth motif, that can be broken up into two disjoint smooth motifs (Fig. 7c). The other motifs (Fig. 7d-f) are associated with paths that cross multiple fold singularities and can be formed by concatenation (Fig. 7g-i). For instance, consider the pair of irreversible paths that is observed, e.g., on the path between  $\vec{e}_b = (1001)$  and  $(1011)$  (Fig. 7d and Fig. 6). Following the configuration along this path reveals two fold singularities (Fig. 7g), so that this motif is composed from a pair of fold motifs. Similarly, other complex motifs (Fig. 7e-f) are similarly reducible and composed from

<sup>3</sup> The reverse is not true: for example, the path between a descendant and sibling is also smooth even though it crosses a fold line, but if the corresponding ancestor is not observed, this path cannot be distinguished from a simple smooth motif.

<sup>4</sup> As before, the reverse is not necessarily true.

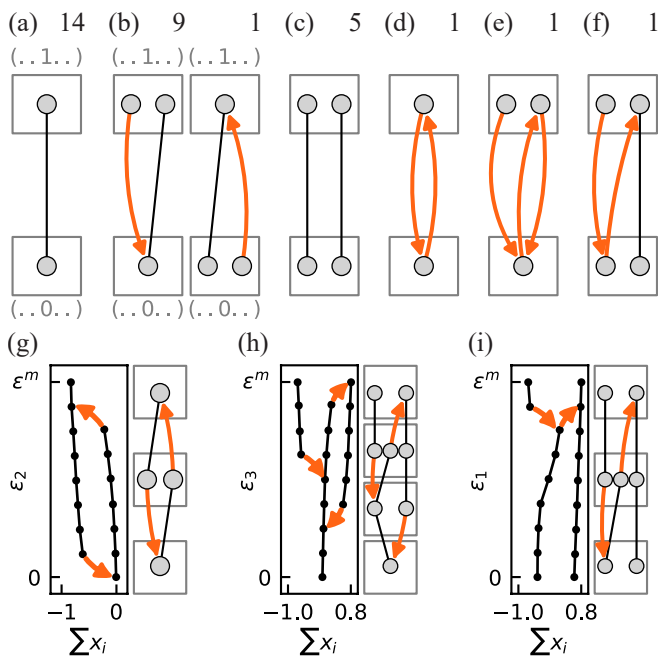


FIG. 7. (a-f) The edge motifs of sample B at  $\epsilon^M = 0.035$ . The top-right number indicates how often these are observed out of 32, showing that smooth (a) and fold (b) motifs are most frequent. Note that while in (a-b) we indicate the binary strains  $(\dots 0 \dots)$   $(\dots 1 \dots)$ , we omit these in further panels as we do not distinguish between increasing and decreasing strains (i.e., the two examples in (b) are equivalent). (c) The double smooth motif is a juxtaposition of two smooth motifs, and thus reducible. (d-f) Three more complex, reducible edge motifs occurring once in the b-graph. (g-i) We follow the evolution of the corresponding configurations along the strain paths of motifs (d-f) and characterize the configurations by collective coordinate  $\sum x_i$  (strain paths between  $[b_i = [(1001), (1101)]$  (g),  $[(1001), (1011)]$  (h), and  $[(0011), (1011)]$  (i)). In each case we find that the evolution along these paths combines two or three fold motifs (left panels), so that we can compose the motif from more elementary smooth and fold motifs (right panels). Note that, although the two fold singularities in (i) occur in the same experimental interval, these are independent events.

smooth and fold motifs (Fig. 7h-i). These examples illustrate that, as generic paths only cross fold singularities, any edge motif observed is composed of smooth and fold motifs, highlighting their fundamental role.

## 2. Loop motifs

We now consider loop motifs, which probe non-trivial path dependencies unique to vectorial strain inputs by involving two ‘active’ beams and while keeping all other strains constant. As before, we consider two motifs equivalent under permutations of the two active beams and flipping of compressions and decompressions. By extracting all loop motifs from the b-graph of sample B, we iden-

tify 13 distinct loop motifs, which include those observed for two-beam sample A (Fig. 8). Note that six of these motifs feature no-return configurations. These configurations feature no incoming transitions within the loop, and can only be reached by strain protocols involving the passive beams (Fig. 8). We stress that each of these represent a distinct sequential logical operation, and discuss the emergent computational power of this system in section VI.

While all edge motifs can be constructed from just two irreducible motifs - smooth and fold motifs - the situation for loop motifs is significantly more complex. To identify the irreducible loop motifs, we focus on those that persist when the size of the loop in strain space is shrunk, and consider all different arrangements of fold curves that cross the four edges composing a loop. Apart from the trivial loop where all edges are smooth, there are three generic possibilities for the arrangements of the fold curves: either the loop is intersected by a single fold curve, the loop contains two fold curves that intersect within the loop, or the loop contains two fold curves that terminate in a higher order cusp singularity. All irreducible loop motifs can then be constructed starting from the combinatorics of the fold curves intersecting different edges — however, this construction is not trivial. Without going into too much detail, we note that fold curves have an orientation (on which side lies the ancestor node), cusp structures can correspond to both supercritical and subcritical bifurcation which lead to different motifs, and irreversible transitions can connect to multiple different descendants. We estimate that there are significantly more than 20 of such irreducible loop motifs.

## VI. EMERGENT MEMORY AND COMPUTING

We now discuss the path-dependent response under vectorial driving from two perspectives: as an emergent phenomenon that leads to novel memory effects that allows to understand and classify disordered media (Sec. VIA), and as a new avenue towards *in materia* computing (Sec. VIB).

### A. Transient responses

The response to cyclic driving provides an important fingerprint of the memory effects of complex systems [2–4, 9, 10, 12–28, 32, 33, 42, 43]. For scalar cyclic driving, deterministic, dissipative, multistable systems must settle in a periodic response after a finite number of cycles [9, 10, 12–24, 27]. For a wide class of systems that can be seen as composed of weakly interacting elements, the response satisfies so-called Return Point Memory which forbids the presence of transients longer than one cycle [28, 44]. Recent observations of finite transients, in, e.g.,

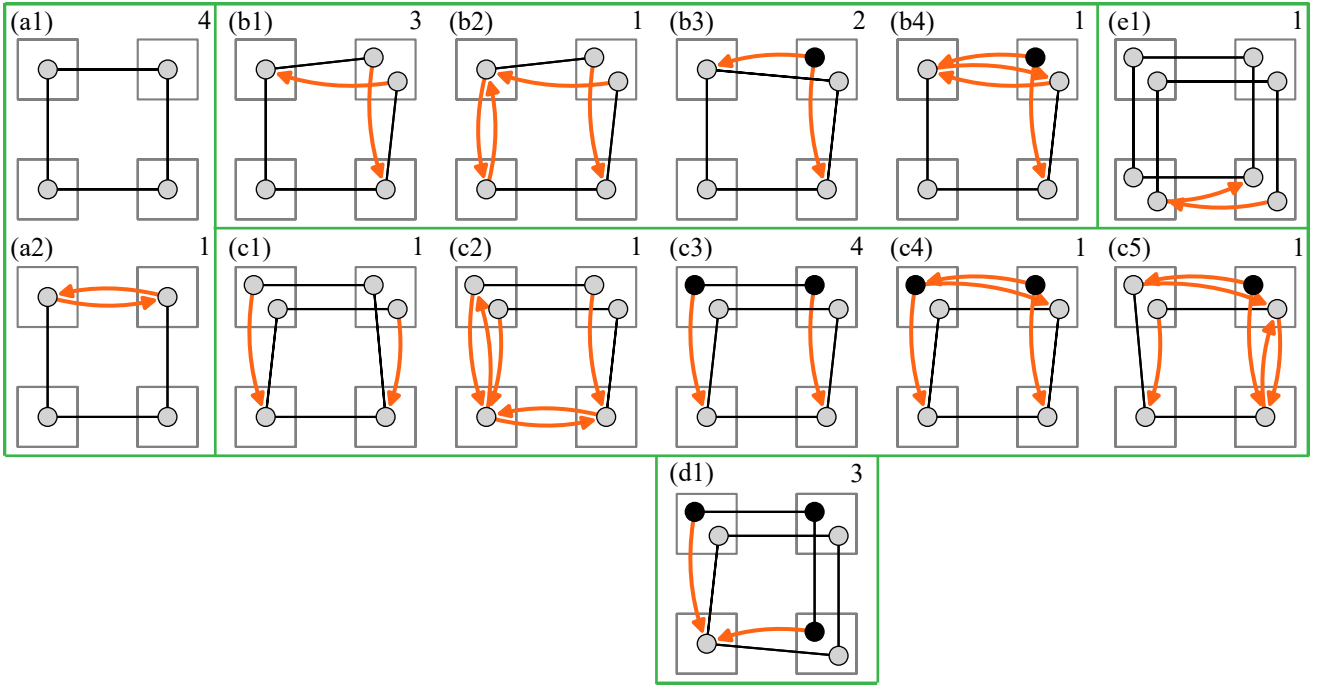


FIG. 8. The loop motifs of sample B at  $\varepsilon^M = 0.035$ . The black nodes lack an incoming connection in the motif, and correspond to 'no-return' configurations in their specific motif. We group the motifs by their number of configurations, and orient these such that the larger number of configurations are to the right and top. Five of these motifs (a1,b1,b3,c3,d1) occur more than once in sample B, indicated by the top-right number.

disordered media and metamaterials, are thus a hallmark of complex memory [9, 10, 12–24, 27].

Here we analyze the edge and loop motifs of sample B from the perspective of transient responses. We first discuss the transients captured in edge-motifs, which are equivalent to the transients under scalar driving, and then introduce loop-transients. We find that edge and loop transients can occur independently, and that the presence of loop transients may depend on the orientation of the driving loops. Vectorial or multi-input driving thus opens a new window on a wider diversity of complex memory effects.

First, edge motifs capture cyclic driving of a strain  $\varepsilon_k$ , and yield a sequence of configurations  $c_0 \rightarrow c_1 \rightarrow c_2 \dots$  that must repeat. The index of the first repeating configuration,  $t_e$ , defines the *transient time*  $\tau_e := t_e/2$  – for example, for a sequence of configurations  $\Gamma_0 \rightarrow \Gamma_1 \rightarrow \Gamma_2 \rightarrow \Gamma_1 \rightarrow \dots$ ,  $\tau_e = 1/2$  [9, 10, 12–24, 27]. Clearly, the smooth motif leads to  $\tau_e = 0$  and the fold motif can produce  $\tau_e = 1/2$ , provided the initial configuration is the ancestor (Fig. 7b). In composite motifs, which involve two or more folds, in our examples  $\tau_e = 0, 1/2$ , and 1 respectively (Fig. 7d-f).

Next, we turn to loop motifs and the response to loop-cyclic strain paths that involve two 'active' beams — notice that such loop-cyclic paths can be clockwise or counterclockwise. We define the loop transient time as  $\tau_l := t_l/4$ , where  $t_l > 0$  is the index of the first repeating configuration. With the exception of two very

simple loop-motifs (Fig. 8a), all others exhibit non-zero loop transients. Starting from a no-return configuration,  $\tau_l \geq 1/4$ , and the longest transient observed is ( $\tau_l = 1$ ) (Fig. 8e).

Loop-transients exhibit properties that have no counterparts in transients under scalar driving. First,  $\tau_l$  often depends on the loop-orientation, e.g., starting from one of the bistable configurations of the cusp motif,  $\tau_l$  is either 0 or  $1/4$  (Fig. 8b1). Second, this example illustrates that a non-zero loop-transient can occur along a totally smooth and reversible path — something that is impossible along linear paths. Finally, the presence of loop and edge transients is decoupled. We illustrate this for the cusp-motif (Fig. 8b1 and 9). Starting from the top node in the bistable region, for the CCW loop-cyclic path  $\tau_l = 1/4$ , while an edge-cyclic path starting in the same direction has  $\tau_e = 0$  — similarly, the CW loop-cyclic path leads to  $\tau_l = 0$ , while the corresponding edge-cyclic path yields  $\tau_e = 1/2$ .

## B. Tunable emergent computation

The complex response of multistable materials with multiple inputs opens a route to tunable computation. In our example of sample B, the loop motifs already uncover a wide range of different sequential logic circuits, but here we focus on the aspects of reprogrammability, where we use two inputs, e.g. 1 and 3, to tune the sequential logical

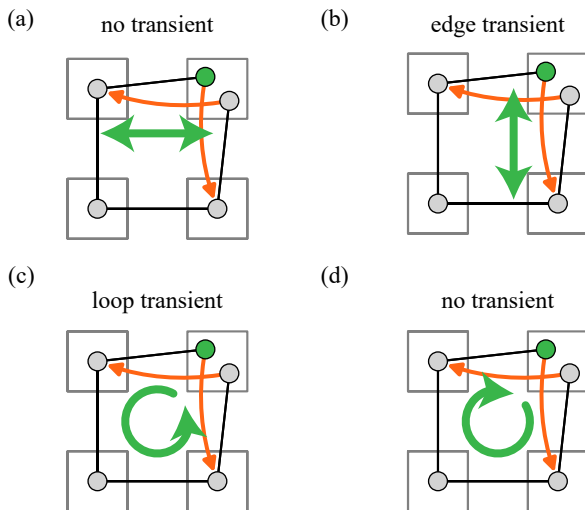


FIG. 9. Illustration of the impact of orientation on the transient time. We focus on a single motif, and transient times under scalar and loop actuation (green arrow) starting from a given configuration (green circle). (a-b) The transient response of an edge-cyclic strain path depends on the edge; in (a),  $\tau_e = 0$ ; in (b)  $\tau_e = 1/2$ . (c-d) The transient response of a loop-cyclic strain path depends on the orientation of the loop. (in (c),  $\tau_l = 1/4$ ; in (d)  $\tau_l = 0$ .)

operations on two other inputs, e.g., 2 and 4 (Fig. 10). For this example, compressing the programming beams enables the selection of four distinct mechanical algorithms that operate on the input beams. Hence, high-dimensional input spaces allow for allocating specific input dimensions to tune the *in materia* computing properties of the remaining input dimensions. While a similar strategy has been used to obtain reprogrammable logical circuits in disordered electronic materials with multiple terminals, we believe that our example illustrates that multistable systems naturally allow for sequential operations that mix logic and memory [45–48]. In general, we expect that these computations can be captured by finite state machines [24], where it is an open question how the number of states, input characters and computational capabilities grow with the dimensionality of the driving input.

We point out that a wider variety of more powerful computations can be realized by using more complex driving protocols, samples with different interaction strength  $k$ , and more complex geometries with more inputs. First, relaxing the constraints that the minimal input strains,  $\varepsilon_i^m$  are zero and the maximal input strains,  $\varepsilon_i^M$  are equal, naturally expands the space of computations and reprogrammabilities. Similarly, more information can be encoded using non-binary driving sequences, pushing the computational power of our multistable samples in the direction of finite state machines with many states and input characters [24]. Second, in numerical simulations we have observed that for lower values of  $k$ , the number of stable configurations per strain can reach

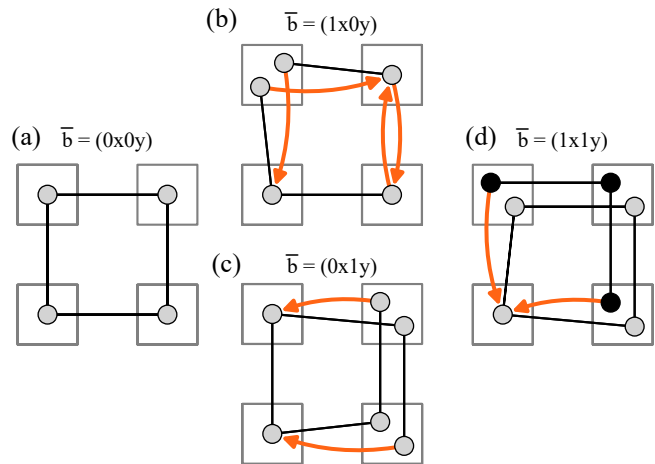


FIG. 10. Loop motifs of sample B at  $\varepsilon^M = 0.035$  with active beams 2 and 4 and distinct tuning beams. In this representation the strains on the active beams 1 and 3 correspond to the  $x$  and  $y$  direction in the motifs, and the binary strains on the passive beams  $b_1, b_3$  is 0 or 1, as indicated by the labels.

$2^n$ , and the number of reachable configurations is at least five. Hence, such samples would allow for longer and more varied transients and multi-bit sequential operations. Finally, our chain geometry encodes specific interactions, and planar or fully connected geometries may encode more complex computations.

## VII. CONCLUSION AND OUTLOOK

Vectorial driving allows to uncover a wealth of path-dependent responses, providing insight into the complexity of frustrated materials. We show that underpinning these are fold-singularities, which lead to ADS triplets that form the basis of graph-based descriptions of the sequential response. For scalar driving, pairs of ADS triplets form elementary hysteresis loops (hysterons) [5, 9, 10, 14, 23–26, 28–32], whereas in higher-dimensional driving spaces, more diverse connections between ADS triplets lead to rich path-dependencies. We further introduce binarization as an effective, simplified driving strategy to reveal new memory effects and computational capabilities. Together, vectorial driving opens new avenues for characterizing frustrated systems, uncovering novel multi-dimensional responses and memories, and advancing strategies for powerful *in-materia* computing [48].

More broadly, the historic increase in complexity of measured data in physical experiments - from scalar data to images, and from static to dynamic data - has not yet been matched by a similar increase in the complexity of driving protocols. The recent focus on experimentally accessible sequential driving protocols [33] - which do not require new experimental techniques for detection - is an

important step in this direction, opening up the study of memory effects in response to time-ordered input. We believe that, sequential vectorial driving is similarly ripe for wide implementation in experiments and simulations. One particular promising direction is in *in-materia* computing, where, e.g., multiterminal electronic devices naturally allow for such driving [46], and it will be exciting to translate our concepts to other domains and applications.

We note that our work is related but distinct from recent work that considers, e.g., shear in different directions [51–57], uniaxial compression in different directions [37], or sequential application of compression and then shear [58–60]; what new phenomena occur for sequential driving paths that combine two or more components of the strain?

Finally, vectorial driving allows a new window on complex materials. For example, probing the (non-Abelian) response as function of the distance between two driving locations, can reveal a characteristic lengthscale [41]. Moreover, we expect a wealth of new memory effects, such as multiperiodic responses under loop-like driving paths [2, 9, 12, 13, 15–21, 23], and higher-dimensional equivalences of return-point memory [9, 10, 12, 13, 25, 26, 28].

#### ACKNOWLEDGEMENTS

CM and MvH acknowledge funding from European Research Council Grant ERC-101019474. We thank M. Teunisse and Y. Shokef for fruitful discussions and J. Mesman, D. Ursem, H.J. Boluijt, and R. Zwart for technical support.

- 
- [1] S. Slotterback, M. Mailman, K. Ronaszegi, M. van Hecke, M. Girvan, W. Losert, Onset of irreversibility in cyclic shear of granular packings, *Phys. Rev. E* **85**, 021309 (2012).
- [2] J. D. Paulsen, N. C. Keim and S. R. Nagel, Multiple transient memories in experiments on sheared non-Brownian suspensions, *Phys. Rev. Lett.* **113**, 068301 (2014).
- [3] M. Adhikari, S. Sastry, Memory formation in cyclically deformed amorphous solids and sphere assemblies, *Eur. Phys. J. E Soft Matter* **41**, 105 (2018).
- [4] N. C. Keim, J. Hass, B. Kroger and D. Wieker, Global memory from local hysteresis in an amorphous solid, *Phys. Rev. Res.* **2**, 012004, (2020).
- [5] I. Regev, I. Attia, K. Dahmen, S. Sastry, M. Mungan, Topology of the energy landscape of sheared amorphous solids and the irreversibility transition, *Phys. Rev. E* **103**, 062614 (2021)
- [6] K. Matan, R. B. Williams, T. A. Witten, S. R. Nagel, Crumpling a thin sheet, *Phys. Rev. Lett.* **88**, 076101 (2002).
- [7] H. Aharoni, E. Sharon, Direct observation of the temporal and spatial dynamics during crumpling, *Nature Materials* **9**, 993 (2010).
- [8] Y. Lahini, O. Gottesman, A. Amir, S. M. Rubinstein, Nonmonotonic aging and memory retention in disordered mechanical systems, *Phys. Rev. Lett.* **118**, 085501 (2017).
- [9] H. Bense and M. van Hecke, Complex pathways and memory in compressed corrugated sheets, *Proc. Natl. Acad. Sci. U. S. A.* **118**, e2111436118 (2021).
- [10] D. Shohat, D. Hexner, and Y. Lahini, Memory from coupled instabilities in unfolded crumpled sheets, *Proc. Natl. Acad. Sci. U. S. A.* **119**, e2200028119 (2022).
- [11] A. S. Meeussen and M. van Hecke, Multistable sheets with rewritable patterns for switchable shape-morphing, *Nature* **621**, 516-520 (2023).
- [12] N. C. Keim, J. D. Paulsen, Z. Zeravcic, S. Sastry and S. R. Nagel, Memory formation in matter, *Rev. Mod. Phys.* **91**, 035002 (2019).
- [13] J. D. Paulsen and N. C. Keim, Mechanical memories in solids, from disorder to design, *Annual Reviews* **16**, 032822-035544 (2024).
- [14] C. W. Lindeman and S. R. Nagel, Multiple memory formation in glassy landscapes, *Sci. Adv.* **7**, eabg7133 (2021).
- [15] I. Regev, T. Lookman, C. Reichardt, Onset of irreversibility and chaos in amorphous solids under periodic shear, *Phys. Rev. E*, **88**, 062401 (2013).
- [16] C.F. Schreck, R.S. Hoy, M.D. Shattuck, C.S. O'Hern, Particle-scale reversibility in athermal particulate media below jamming, *Phys. Rev. E* **88**, 052205 (2013).
- [17] J.R. Royer, P.M. Chaikin, Precisely cyclic sand: Self-organization of periodically sheared frictional grains, *Proc. Natl. Acad. Sci. U. S. A.* **112**, 49-53 (2015).
- [18] T. Kawasaki, L. Berthier, Macroscopic yielding in jammed solids is accompanied by a nonequilibrium first-order transition in particle trajectories, *Phys. Rev. E* **94**, 022615 (2016).
- [19] M.O. Lavrentovich, A.J. Liu, S.R. Nagel, Period proliferation in periodic states in cyclically sheared jammed solids. *Phys. Rev. E* **96** 020101 (2017).
- [20] K. Nagasawa, K. Miyazaki, T. Kawasaki, Classification of the reversible-irreversible transitions in particle trajectories across the jamming transition point. *Soft Matt.* **15**, 7557-7566 (2019).
- [21] W. Yeh, M. Ozawa, K. Miyazaki, T. Kawasaki, L. Berthier, Glass stability changes the nature of yielding under oscillatory shear. *Phys. Rev. Lett.* **124**, 225502 (2020).
- [22] L.J. Kwakernaak, M. van Hecke, Counting and sequential information processing in mechanical metamaterials, *Phys. Rev. Lett.* **130**, 268204 (2023).
- [23] N. C. Keim and J. D. Paulsen, Multiperiodic orbits from interacting soft spots in cyclically sheared amorphous solids, *Sci. Adv.* **7**, eabg7685 (2021).
- [24] J. Liu, M. Teunisse, G. Korovin, I. R. Vermaire, L. Jin, H. Bense, M. van Hecke, Controlled pathways and sequential information processing in serially coupled mechanical hysterons, *Proc. Natl. Acad. Sci. U. S. A.* **121**, e2308414121 (2024).
- [25] M. Mungan, M. M. Terzi, The Structure of State Transition Graphs in Systems with Return Point Memory: I. General Theory, *Ann. H. Poincare* **20**, 2819 (2019).
- [26] M. Mungan, S. Sastry, K. Dahmen and I. Regev, Networks and hierarchies: How amorphous materials learn to remember, *Phys. Rev. Lett.* **123**, 178002 (2019).
- [27] J. D. Paulsen and N. C. Keim, Minimal descriptions of cyclic memories, *Proc. R. Soc. A* **475**, 20180874 (2019).
- [28] M. M. Terzi, M. Mungan, State transition graph of the Preisach model and the role of return-point memory, *Phys. Rev. E* **102** 012122 (2020).
- [29] M. van Hecke, Profusion of transition pathways for interacting hysterons, *Phys. Rev. E* **104**, 054608 (2021).
- [30] D. Melancon, A. Elia Forte, L. M. Kamp, B. Gorissen, K. Bertoldi, Inflatable Origami: Multimodal Deformation via Multistability, *Adv. Funct. Mater.* **32**, 2201891 (2022).
- [31] T. Jules, A. Reid, K. E. Daniels, M. Mungan F. Lechenault, The delicate memory structure of coupled origami switches, *Phys. Rev. Research* **4**, 013128 (2022).
- [32] J. Ding, M. van Hecke, Sequential snapping and pathways in a mechanical metamaterial, *J. Chem. Phys.* **156**, 204902 (2022).
- [33] C. W. Lindeman, T. R. Jalowiec and N. C. Keim, Generalizing multiple memories from a single drive: The hysteron latch, *Sci. Adv.* **11**, eadr5933 (2025).
- [34] M. Mozaffar, R. Bostanabad, W. Chen, K. Ehmann, J. Cao and M.A. Bessa, Deep learning predicts path-dependent plasticity, *Proc. Natl. Acad. Sci. U.S.A.* **116** (52) 26414-26420 (2019).
- [35] X. Guo, M. Guzmán, D. Carpentier, D. Bartolo, C. Coulais, Non-orientable order and non-commutative response in frustrated metamaterials, *Nature* **618** 506 (2023).
- [36] C. Sirote-Katz, D. Shohat, C. Merrigan, Y. Lahini, C. Nisoli, Y. Shokef, Emergent disorder and mechanical memory in periodic metamaterials, *Nat. Comm.* **15** 4008 (2024).
- [37] B. Florijn, C. Coulais, M. van Hecke, Programmable Mechanical Metamaterials, *Phys. Rev. Lett.* **113** 175503 (2024)
- [38] C. M. Meulblok and M. van Hecke, Path dependency: generic and non-generic paths, in preparation.

- [39] M. H. Teunisse and M. van Hecke, Transition graphs of interacting hysterons: structure, design, organization and statistics, arXiv 2404.11344 (2024).
- [40] P. Horowitz, W. Hill, I. Robinson, The Art of Electronics Vol. 2, Cambridge Univ. Press (1989).
- [41] C. M. Meulblok, A. Singh and M. van Hecke, Edge and loop motifs in multistable materials, in preparation.
- [42] N. C. Keim, S. R. Nagel, Generic Transient Memory Formation in Disordered Systems with Noise, *Phys. Rev. Lett.* **107**, 010603 (2011).
- [43] V. F. Hagh, S. R. Nagel, A. J. Liu, L. M. Manning, E. I. Corwin, Transient learning degrees of freedom for introducing function in materials, *Proc. Natl. Acad. Sci. U. S. A.* **119** e2117622119 (2022).
- [44] J. P. Senthia, K. Dahmen, S. Kartha, J. A. Krumhansl, B. W. Roberts, J. D. Shore, Hysteresis and hierarchies: Dynamics of disorder-driven first-order phase transformations, *Phys. Rev. Lett.* **70**, 3347 (1993).
- [45] M. Serra-Garcia, Turing-complete mechanical processor via automated nonlinear system design, *Phys. Rev. E* **100**, 042202 (2019).
- [46] T. Chen, J. van Gelder, B. van de Ven, S. V. Amitonov, B. De Wilde, H.-C. Ruiz Euler, H. Broersma, P. A. Bobbert, F. A. Zwanenburg, W. G. van der Wiel, Classification with a disordered dopant-atom network in silicon, *Nature* **577**, 341 (2020).
- [47] C. El Helou, B. Grossmann, C. E. Tabor, P. R. Buskohl and R. L. Harne, Mechanical integrated circuit materials, *Nature* **608**, 699 (2022).
- [48] C. Kaspar, B. J. Ravoo, W. G. van der Wiel, S. V. Wegner and W. H. P. Pernice, The rise of intelligent matter, *Nature* **594**, 345 (2021).
- [49] T. Yang, D. Hathcock, Y. Chen, P. L. McEuen, J. P. Sethna, I. Cohen, I. Griniasty, Bifurcation instructed design of multistate machines, *Proc. Natl. Acad. Sci. U. S. A.* **120** e2300081120 (2023).
- [50] J. T. B. Overvelde, T. Kloek, J. J. A. D'haen, K. Bertoldi, Amplifying the response of soft actuators by harnessing snap-through instabilities, *Proc. Natl. Acad. Sci. U. S. A.* **112** 10863 (2022).
- [51] S. Dagois-Bohy, B. P. Tighe, J. Simon, S. Henkes and M. van Hecke, Soft-sphere packings at finite pressure but unstable to shear, *Phys. Rev. Lett.* **109**, 095703 (2012).
- [52] C. P. Goodrich, S. Dagois-Bohy, B. P. Tighe, M. van Hecke, A. J. Liu and S. R. Nagel, Jamming in finite systems: stability, anisotropy, fluctuations, and scaling, *Phys. Rev. E* **90**, 022138 (2014).
- [53] O. Gendelman, P. K. Jaiswal, I. Procaccia, B. Sen Gupta and J. Zylberg, Shear transformation zones: state determined or protocol dependent?, *Europhysics Letters* **109**, 16002 (2015).
- [54] S. Patinet, D. Vandembroucq and M. L. Falk, Connecting local yield stresses with plastic activity in amorphous solids, *Phys. Rev. Lett.* **117**, 045501 (2016).
- [55] A. Barbot, M. Lerbinger, A. Hernandez-García1, R. García-García1, M. L. Falk, D. Vandembroucq and S. Patinet, Local yield stress statistics in model amorphous solids, *Phys. Rev. E* **97**, 033001 (2018).
- [56] E. M. Schwem, M. Ramaswamy, C.-M. Cheng, L. Jan and I. Cohen, Embedding orthogonal memories in a colloidal gel through oscillatory shear, *Soft Matter* **16**, 3746-3752 (2020).
- [57] C. W. Lindeman, Multi-dimensional memory in sheared granular materials, arXiv 2407.14966 (2024).
- [58] C. S. O'Hern, L. E. Silbert, A. J. Liu and S. R. Nagel, Jamming at zero temperature and zero applied stress: The epitome of disorder, *Phys. Rev. E* **68**, 011306 (2003).
- [59] M. van Hecke, Jamming of soft particles: geometry, mechanics, scaling and isostaticity, *J. Phys.: Condens. Matter* **22**, 033101 (2009).
- [60] A. J. Liu and S. R. Nagel, The jamming transition and the marginally jammed solid, *Annual Reviews* **1**, 347-369 (2010).

## APPENDIX A: EXPERIMENTAL DETAILS

### 1. Geometry and Fabrication

Our samples A and B are fabricated by pouring degassed Mold Star 30 silicone rubber (Young's modulus of  $\approx 1$  MPa, Poisson's ratio of  $\approx 0.5$ ) into open face molds that are 3D printed on UltiMaker S3 printers. The samples are cured at room temperature. After curing, the samples are removed by breaking the molds carefully.

Sample A features two units and sample B features four units; both have the same beam parameters ( $t = 3.5$  mm,  $\delta = 0.08$ ), a thickness of 10 mm to prevent out-of-plane buckling, and tapered connections to minimize torsional effects (Fig. 11a). We embedded an elliptical annulus ( $w_b = 12$  mm,  $l_b = 20$  mm,  $w_s = 8$  mm and  $l_s = 16$  mm) in the horizontal beam to lower its spring constant (Fig. 11b). Each unit is terminated by a rectangular block that allows to attach the sample to the compression device (Fig. 11c). Finally, we use 2.5 mm diameter protrusions that are painted white to track the real-space configuration (Sec. 3).

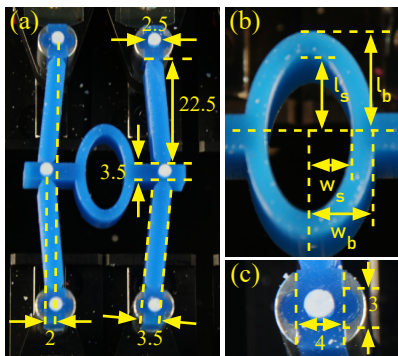


FIG. 11. Sample geometry; all dimensions in millimeters, errorbar  $\pm 0.1$  mm. (a) Sample A with two units, (b) Zoom in on elliptical annulus. (c) Zoom in on terminating block.

### 2. Measuring Effective Coupling

We measured the mechanical response of the vertical beam and horizontal spring to determine the effective interaction coefficient  $k = k_h/k_v$  of our samples. We fabricate separated vertical units and elliptical spring units using the same 3D-printing and molding techniques, and probe their force-compression response  $F(U)$  in an uniaxial testing device (Instron type 5965), which controls the compression  $U$  better than  $10^{-3}$  mm and allows us to measure the compressive force  $F$  with an accuracy  $10^{-4}$  N. We use linear fits to  $F(U)$  and find that  $k_v = 9.17 \pm 0.01 \cdot 10^2$  N/m and  $k_h = 81 \pm 5$  N/m, leading to  $k \approx 0.09$ .

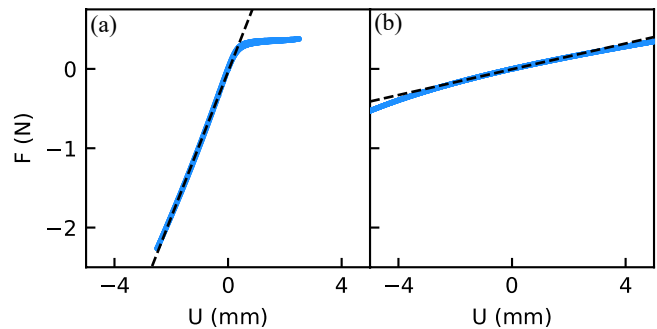


FIG. 12. Mechanical response of a vertical beam (a) and horizontal spring (b) and linear fits (dashed lines). The vertical spring buckles at large compression ( $U > 0.7$  mm) - in our path dependent experiments, we do not reach this limit - and we restrict the fit to the domain  $U \in [-2 \text{ mm}, 0.5 \text{ mm}]$  - The dashed lines represent linear fits.

### 3. Driving

We use a custom-made compression device to individually control the compression on each beam. The beams are symmetrically compressed from both top and bottom to ensure horizontal alignment of the middle nodes. The compression is controlled by a DC servo motor actuator (Thorlabs Z825B), providing an accuracy of 0.01 mm and a repeatability of 0.01 mm. To maintain operation within the quasi-static limit, the compression rate is set to 0.1 mm/s, with a maximal acceleration of 3 mm/s<sup>2</sup>. During each compression sequence, snapshots of the metamaterial configuration are captured using a CCD camera (Basler acA2040-90um, 12.9 pixel/mm). From the snapshots, the node positions are extracted using standard python image analysis packages, achieving an accuracy of 0.005 of the dimensionless quantities  $\vec{x}$ .

## APPENDIX B: NUMERICAL DETAILS

Complementary to experiments, we use a numerical spring model. We define the elastic energy  $E(x_i)$  by approximating each biased beam with two (nearly) vertical springs with spring constants  $k_v$  and rest length  $l_0 = \sqrt{1 + \delta^2}$ , where  $\delta$  is the bias of the beam. The energy of each vertical spring reads:

$$E_{v,i} = \frac{1}{2}(l - l_0)^2 = \frac{1}{2} \left( \sqrt{(1 - \varepsilon_i)^2 + x_i^2} - \sqrt{1 + \delta^2} \right)^2, \quad (2)$$

where,  $x_i$  is the position of the middle of the beam with respect to the clamped-clamped boundaries and  $2\varepsilon_i$  is the compressive strain. The horizontal spring has alternating rest length  $1 - (-1)^i 2\delta$  and spring constant  $k_h$  and energy:

$$E_{h,i} = \frac{k}{2}(x_i - x_{i+1} - 2\delta)^2. \quad (3)$$

As each unit in our system consists of two vertical springs, we obtain a total energy:

$$E = \sum_{i=1}^n \left( \sqrt{(1 - \varepsilon_i)^2 + x_i^2} - \sqrt{1 + \delta^2} \right)^2 + \dots \\ \sum_{i=1}^{n-1} \frac{k}{2} (x_i - x_{i+1} - (-1)^i 2\delta)^2. \quad (4)$$

where  $k := k_h/k_v$  is the ratio between the horizontal and vertical spring constants.

We obtain equilibrium positions of  $\{x_i\}$  given a strain  $\vec{\varepsilon}$  by finding the roots of the forces  $F_i = \partial_{x_i} E$  using the Newton-Raphson method. Each strain-driving step is divided into several small steps of  $10^{-5}$  to mimic the quasi-static dynamics and to allow to distinguish between smooth and non-smooth deformations.

In the lowest order, the energy simplifies to:

$$E = \sum_{i=1}^n \left( \frac{x_i^2}{2} - \gamma_i \right)^2 + \sum_{i=1}^{n-1} \frac{k}{2} (x_i - x_{i+1} - (-1)^i 2\delta)^2, \quad (5)$$

where  $\gamma_i := \varepsilon_i + \delta^2/2 - \varepsilon_i^2/2 \approx \varepsilon_i + \delta^2/2$ . Hence, our model system essentially consists of coupled quartic potentials. In the small strain limit ( $\varepsilon_i^2 \approx 0$ ), this approximation of  $E$  can be rescaled such that the bias  $\delta$  drops out:

$$x_i \rightarrow \delta x'_i, \quad (6)$$

$$\varepsilon_i \rightarrow \delta^2 \varepsilon'_i, \quad (7)$$

$$k \rightarrow \delta^2 k, \quad (8)$$

$$E \rightarrow \delta^4 E', \quad (9)$$

resulting in:

$$E' = \sum_{i=1}^n \left( \frac{x_i'^2}{2} - \varepsilon_i - \frac{1}{2} \right)^2 + \sum_{i=1}^{n-1} \frac{k}{2} (x_i - x_{i+1} - (-1)^i 2)^2. \quad (10)$$

Hence, in lowest order, the coupling strength  $k$  is the only system parameter.

### APPENDIX C: CONFIGURATIONS NEAR CUSP

Here, we detail the real-space configurations in the bistable domain near the cusp/pitchfork  $Q$ . So far, we have associated the non-Abelian response with  $B_1$  and  $B_2$  being 'left-leaning' or 'right-leaning' for sample A (see Sec. II B). However, near the pitchfork bifurcation  $Q$ , the configurations associated with  $B_1$  and  $B_2$  both have  $x_1 < 0$  and  $x_2 > 0$ , and are thus not 'left-leaning' or 'right-leaning' (Fig. 13). As a result, the binary projection of  $\vec{x}$  does not capture the bistability in this (small) domain (Fig. 13a).

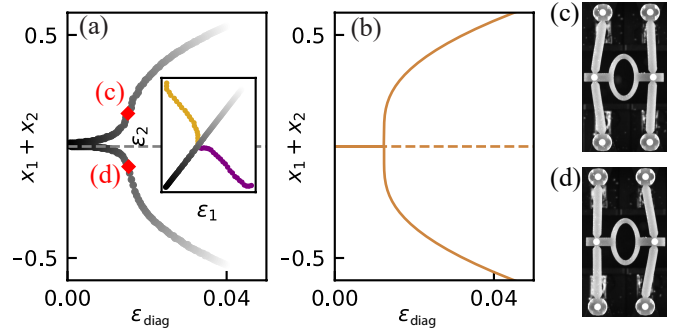


FIG. 13. Pitchfork bifurcation observed along a non-generic strain path through a cusp singularity. (a) The collective coordinate  $x_1 + x_2$  along a diagonal strain path ( $\varepsilon_1 = \varepsilon_2 := \varepsilon_{\text{diag}}$ , inset) starting from  $\varepsilon_{\text{diag}} = 0.04$  and ending at  $\varepsilon_{\text{diag}} = 0$  (sample A). (b) Results from spring model ( $k = 0.09$  and  $\delta = 0.08$ ) along the same path. (c-d) Snapshots of the system corresponding to the red dots indicated in panel (a); note that in both cases, the left beam is left leaning and the right beam is right leaning.

### APPENDIX D: BOOLEAN LOGIC DETAILS

Here, we detail the mapping from the five b-graphs, present in sample A, to their Boolean circuits. Recall that for this mapping we project the real-space configuration onto a binary output variable  $\vec{Q} = (q_1 q_2)$ , where  $q_i = 0$  ( $q_i = 1$ ) when  $x_i < 0$  ( $x_i > 0$ ). Furthermore, we introduced a binary input variable  $\vec{b} = (b_1 b_2)$  with  $b_i = 0, 1$ , defining the strain as  $\varepsilon_i = \varepsilon_i^M b_i$ , and consider sequential protocols where  $\vec{b}(t)$  and  $\vec{b}(t-1)$  differ in precisely one location. As explained in the main text, we obtain the five different regimes by varying  $\varepsilon_i^M$ , avoiding the tiny interval  $\varepsilon_c < \varepsilon_i^M < \varepsilon_g$  where the units are not clearly left or right leaning.

To describe the five distinct path dependent responses, we present the relation between  $\vec{b}(t)$ ,  $\vec{b}(t-1)$ ,  $\vec{Q}(t)$  and  $\vec{Q}(t-1)$  in truth tables (Fig. 14). We note that the truth table of the linear regime ( $\varepsilon_i^M < \varepsilon_c$ ) is trivial ( $\vec{Q}(t) = (01)$  irrespective of (previous) inputs). In the four non-trivial truth tables, we highlight cases where  $\vec{Q}(t)$  depends on the previous state in blue (Fig. 14). In the main text, we map these truth tables to logic circuits, although we stress that these circuits are not unique. Finally, we stress a subtle point between ordinary SR latches and our circuits: since the outputs of SR latches usually are supposed to be connected (i.e.  $Q_1 = \neg Q_2$ , the input  $\vec{b} = (00)$  is considered ill-defined - here the outputs are independent, and therefore all inputs are allowed.

### APPENDIX E: EXPERIMENTAL FOUR-BEAM B-GRAPHS

Here, we detail the four-beam b-graph of sample B and provide four additional b-graphs for distinct  $\varepsilon^M$ .

(a) $\vec{b}(t)$	$\vec{b}(t-1)$	$\vec{Q}(t-1)$	$\vec{Q}(t)$	(b) $\vec{b}(t)$	$\vec{b}(t-1)$	$\vec{Q}(t-1)$	$\vec{Q}(t)$	(c) $\vec{b}(t)$	$\vec{b}(t-1)$	$\vec{Q}(t-1)$	$\vec{Q}(t)$	(d) $\vec{b}(t)$	$\vec{b}(t-1)$	$\vec{Q}(t-1)$	$\vec{Q}(t)$
(00)	(xx)	(xx)	(01)												
(01)	(xx)	(xx)	(11)	(01)	(00)	(01)	(11)	(01)	(00)	(01)	(11)	(01)	(xx)	(xx)	(11)
(10)	(xx)	(xx)	(00)	(01)	(11)	(00)	(00)	(01)	(11)	(00)	(00)	(10)	(00)	(01)	(00)
(11)	(01)	(00)	(00)	(01)	(11)	(11)	(11)	(01)	(11)	(11)	(11)	(10)	(11)	(00)	(00)
(11)	(10)	(11)	(11)	(10)	(00)	(01)	(00)	(10)	(xx)	(xx)	(00)	(10)	(11)	(11)	(11)
				(10)	(11)	(00)	(00)	(11)	(01)	(00)	(00)	(11)	(01)	(11)	(11)
				(10)	(11)	(11)	(11)	(11)	(01)	(11)	(11)	(11)	(10)	(00)	(00)
				(11)	(01)	(00)	(00)	(11)	(10)	(00)	(00)	(11)	(10)	(11)	(11)
				(11)	(01)	(11)	(11)	(11)	(10)	(11)	(11)	(11)	(10)	(00)	(00)
				(11)	(10)	(00)	(00)	(11)	(10)	(00)	(00)	(11)	(10)	(11)	(11)
				(11)	(10)	(11)	(11)								

FIG. 14. (a-d) Truth tables of sample A corresponding to the sequential Boolean circuits in Fig. 5b-e, respectively; the table for Fig. 5a is trivial and omitted here. Crosses indicate cases where the values of  $\vec{b}(t-1)$  and  $\vec{Q}(t-1)$  are irrelevant; blue boxes indicate cases where the output depends on the previous state.

Different driving sequences that end in strain  $\vec{b}$  can lead real-space configurations  $\vec{x}$  that are only slightly different. We take two configurations as equivalent if  $\sum_i |x_i(P_k(\vec{b})) - x_i(P_l(\vec{b}))| \leq 0.015$ .

In addition to the b-graph presented in Sec. V for  $\varepsilon^M = 0.035$ , we map the response of sample B for  $\varepsilon^M = 0.03, 0.0325, 0.0375, \text{ and } 0.04$  (Fig. 15). In these responses, we find the same edge motifs and the same loop motifs as in Sec. V. Note that the qualitative response for  $\varepsilon^M = 0.03$ , and  $\varepsilon^M = 0.0325$  is equivalent (Fig. 15a-b). Together, we conclude that high-dimensional b-graphs can be robustly mapped using our recursive strategy.

## APPENDIX F: MOVIE CAPTIONS

**Movie S1:** Non-Abelian response of sample A. We consider pair of sequential driving paths  $P_1 : [c_1, c_2]$  (a) and  $P_2 : [c_2, c_1]$  (b), with  $\varepsilon_i^m = 0$  and  $\varepsilon_i^M = 0.03$ . Scalebar is 5 mm.

**Movie S2:** Mixed-mode response of sample A. We consider pair of sequential driving paths  $P_3 : [d_1, d_2]$  (a) and  $P_4 : [d_2, d_1]$  (b), after an initial driving path  $P_1$ . We take  $\varepsilon_i^m = 0$  and  $\varepsilon_i^M = 0.03$ . Scalebar is 5 mm.

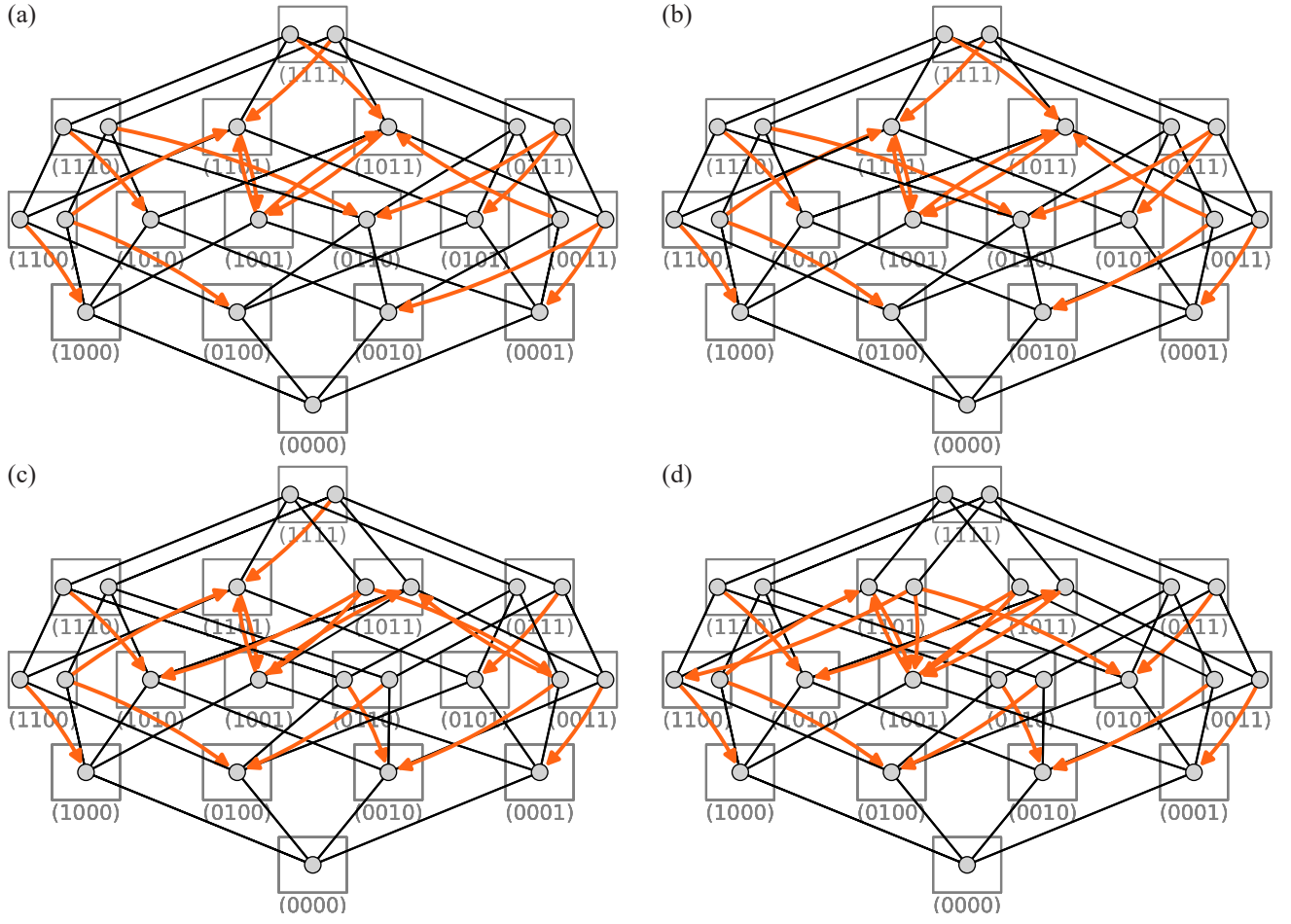


FIG. 15. (a-d) b-graphs of sample B for  $\varepsilon^M = 0.03, 0.0325, 0.0375,$  and  $0.04$  respectively. We note that the b-graph for  $\varepsilon^M = 0.03,$  and  $0.0325$  have the same topology.